Scattering cancellation technique for acoustic spinning objects

Mohamed Farhat,[1,*] Sebastien Guenneau,[2] Andrea Alù,[3] and Ying Wu[1,†]
[1]*Computer, Electrical, and Mathematical Science and Engineering (CEMSE) Division, King Abdullah University of Science and Technology (KAUST), Thuwal 23955-6900, Saudi Arabia*
[2]*UMI 2004 Abraham de Moivre-CNRS, Imperial College London, London SW7 2AZ, United Kingdom*
[3]*Photonics Initiative, Advanced Science Research Center, City University of New York, New York, New York 10031, USA*

(Received 20 March 2020; revised manuscript received 26 April 2020; accepted 29 April 2020; published 20 May 2020; corrected 29 July 2020)

The scattering cancellation technique (SCT) has proved to be an effective way to render static objects invisible to electromagnetic and acoustic waves. However, rotating cylindrical or spherical objects possess additional peculiar scattering features that cannot be canceled by regular SCT-based cloaks. Here, a generalized SCT theory to cloak spinning objects, and hide them from static observers, based on rotating shells with different angular velocity is discussed. This concept is analytically and numerically demonstrated in the case of cylinders, showing that the generalized SCT operates efficiently in making rotating objects appear static to an external observer. Our proposal extends the realm of SCT and brings it one step closer to its practical realization that involves moving objects.

DOI: 10.1103/PhysRevB.101.174111

I. INTRODUCTION

Inspired by the concept of photonic crystals [1–4] and photonic crystal fibers [5–8], a new class of acoustic materials has emerged during the 1990s. These so-called phononic crystals (PCs) consist of a periodic arrangement of at least two materials with different densities [9–12]. These materials were shown to possess a frequency range over which sound-wave propagation is prohibited (phononic band gap) [9,10]. These forbidden bands can also result in singular properties of sound waves, e.g., negative refraction at the interface between a classical medium and a phononic crystal [13–15], ultrasound tunneling [16], or tunable filtering and demultiplexing [17], to cite a few [18–23]. These PCs are difficult to miniaturize, as the band gap appears at wavelengths in the same order as the period of the PCs, meaning a low-frequency band gap requires a large PC [24,25]. To overcome this major hurdle, active research has been directed towards other concepts involving local resonances [26,27] that best operate when the periodicity is much smaller than the wavelength (this is the so-called quasistatic or long-wavelength limit). For instance, composite structures formed by locally resonating meta-atoms, so-called metamaterials (MMs), made their appearance at the turn of the century, both for electromagnetic [28–31] and acoustic [32] waves. Based on analogies drawn from optical MMs, an acoustic MM consists of a heterostructure formed of resonant inclusions having characteristic dimensions smaller than the wavelength of the wave propagating in the medium and vibrating on their natural modes of resonance [33].

Controlling the propagation of waves using these engineered MMs is thus a considerable opportunity [34,35]. For example, we can protect buildings from seismic waves [36,37] or tsunamis [38–41] by means of a large-scale metamaterials, which may guide the acoustic/elastic energy out of the area to be protected and may considerably attenuate the amplitude of the impinging waves or enhance and harvest their energy [42,43]. Defense applications are potentially very important as well, with the possibility, for example, of fabricating stealth systems (invisibility cloaks) [35]. The term "invisibility cloak" designates a coating whose material parameters, determined by the optical transformation process, make it possible to deflect any electromagnetic or elastodynamic wave [44–46]. If we place an object in the isolated interior area, then no incident wave can interact with this object, since the cloak detours wave trajectories around it in such a way that for any external observer the field appears to be undisturbed. In other words, the object is both undetectable (invisible) and protected. Note that the concept of invisibility is distinct from that of stealth [47]. The primary purpose of a stealth coating is to cancel the reflection coefficient in certain directions (typically those of a detection antenna). To do this, the idea is to absorb the incident waves or to reflect them to another direction. Interestingly, some species of moths have acquired dynamic acoustic camouflaging features thanks to some microstructures reminiscent of metamaterial surfaces [48]. Conversely, in an invisible device, we cancel both the reflection coefficient and the absorption, and we make the transmission coefficient ideally unitary. The object included in the coating has then a zero electromagnetic/acoustic size and further has no "shadow" [35]. Other cloaking strategies were subsequently proposed through homogenization [49–51], and/or scattering cancellation technique (SCT) [52,53], and even suggested for other types of waves [54–56].

All the above-mentioned devices and techniques operate for static objects, i.e., at rest. For instance, moving or rotating objects possess intrinsically different scattering signatures

*mohamed.farhat@kaust.edu.sa
†ying.wu@kaust.edu.sa

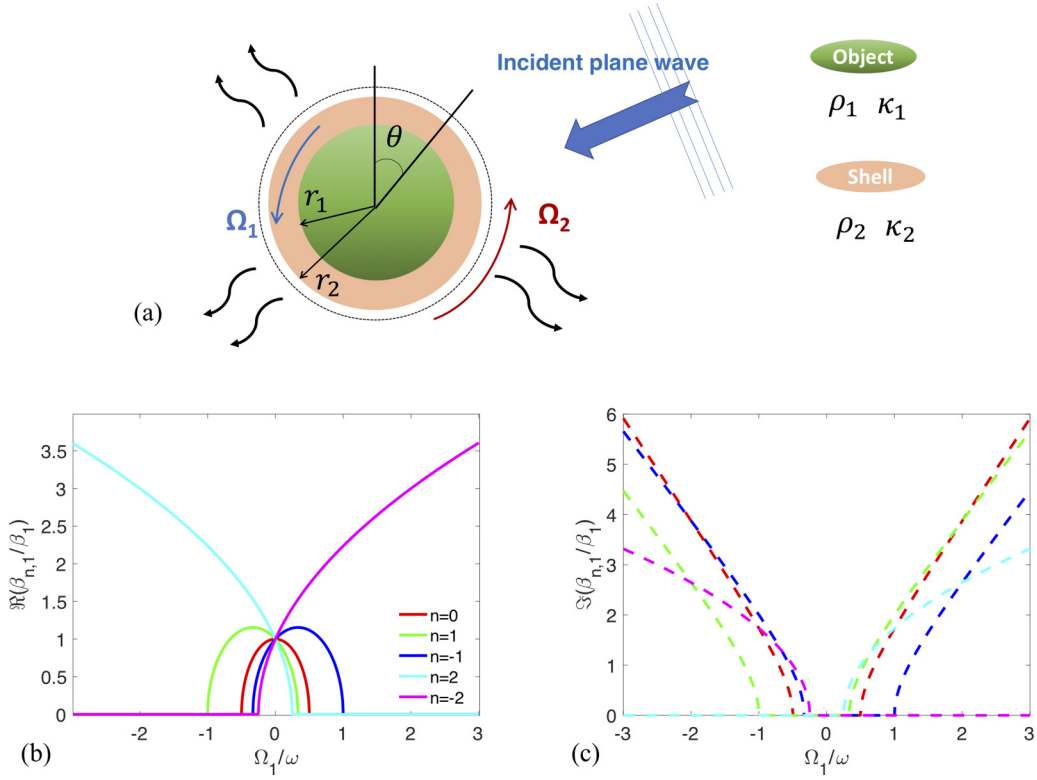

FIG. 1. (a) Scheme of the multiple layers and the interfaces of an acoustic structure, as well as the rotation directions and incident plane wave. (b) Real and (c) imaginary parts of the spinning wave numbers for different orders n vs the rotation coefficient $\alpha_1 = \Omega_1/\omega$.

[57–66] and require special treatment [67,68]. Some intriguing applications were put forward with spinning elements such as gyroscopes [69,70] and waveguide rotation sensors [68]. In order to realize efficient cloaking devices for such rotating devices, we first need to characterize the scattering response from these acoustic objects and then analyze the feasibility and physical difference of a cloaking mechanism. Some recent studies, for example, considered cloaking structures that are moving using spatiotemporal properties to counter the Doppler effect [71–73]. A theory of a space-time cloak was also proposed to make a time interval undetectable for an observer [74] and further demonstrated experimentally in a highly dispersive optical fiber [75]. However, cloaking rotating objects was not achieved in any context. In the present paper, the use of the scattering cancellation technique [53,76–79] to render spinning objects invisible for acoustic waves is proposed.

The rest of the paper is organized as follows. In the background and problem setup section, the equations of motion of a spinning acoustic object and its dispersion relation, which permit the study of acoustic scattering from multilayered spinning structures, are put forward. In the following section, using Bessel expansions of the pressure fields, the possibility of canceling the leading scattering orders from spinning objects by coating them with shells of tailored spinning velocity is shown. In that section, the effect of geometrical parameters and spinning velocity amplitude on the scattering reduction is also analyzed. Finally, the obtained results are summarized in the concluding remarks. Two Appendixes complete the paper with more details on the frequency response and derivation details.

II. BACKGROUND AND PROBLEM SETUP

A. Acoustic equation in rotating media

Let us consider time-harmonic waves, with dependence upon time t proportional to $e^{-i\omega t}$, where ω is the angular wave frequency. We also assume structures with cylindrical invariance [see Fig. 1(a)], i.e., the solution of the physical problem may be expressed in terms of $e^{in\theta}$ so that derivatives in the azimuthal direction θ produce terms of the form in, where n is an integer and $i^2 = -1$. We start by invoking the mass and momentum conservation laws of acoustics, and we express them in the laboratory frame of reference [80]. This is done by using the Eulerian specification of the flow field, i.e., by replacing time derivatives with material derivatives, i.e., $\partial_{t'}(\cdot) \to \partial_t(\cdot) + \mathbf{u}\cdot\nabla(\cdot)$, where the $'$ denotes derivatives taken in the rest frame of the moving fluid. Also, $\mathbf{u} = \mathbf{u}_0 + \mathbf{v}$ is the total velocity of the flow, whereas $\mathbf{u}_0$ is the bulk velocity and $\mathbf{v}$ is the acoustical perturbation velocity. This results in modified conservation equations (see Appendix B).

We combine the modified equations, i.e., Eqs. (B3) and (B4) of Appendix B, by writing down each component [for instance, Eq. (B3) contains two components, while Eq. (B4) contains a single component]. We then use that in cylindrical coordinates $\mathbf{u}_0\cdot\nabla = \Omega_1\partial/\partial\theta$ and linearize the equations by keeping only first-order quantities of acoustic perturbations, e.g., quadratic terms such as $(\mathbf{v}\cdot\nabla)\mathbf{v}$ are neglected, as shown in Appendix B [80]. We thus obtain a linear system (of order 3) in terms of the variables p_1, $v_{r,1}$, and $v_{\theta,1}$ (assuming that the z components of the fields are zero, as it is assumed in this first example, infinitely extended cylinders in the z direction and incidence normal to the z direction). This system of coupled

partial differential equations (PDEs) can be expressed, in cylindrical coordinates, using the differential operator $\tilde{D}$ as $\tilde{D}(v_{r,1}, v_{\theta,1}, p_1)^T = 0$, with $(\cdot)^T$ denoting the transpose of the vector in parentheses, i.e.,

$$\begin{pmatrix} \zeta_{n,1} & -2\Omega_1 & \rho_1^{-1}\partial_r \\ 2\Omega_1 & \zeta_{n,1} & (\rho_1 r)^{-1} in \\ r^{-1}+\partial_r & r^{-1} in & \rho_1^{-1} c_1^{-2} \zeta_{n,1} \end{pmatrix} \begin{pmatrix} v_{r,1} \\ v_{\theta,1} \\ p_1 \end{pmatrix} = \mathbf{0}\,. \quad (1)$$

In this coupled differential system, we denote $\partial_r = \partial/\partial r$ and the modified angular frequency $\zeta_{n,1} = i(n\Omega_1 - \omega)$. From the system of Eq. (1), we derive the equation verified by the pressure p_1 in the cylindrical coordinates, that is,

$$\frac{\partial^2 p_1}{\partial r^2} + \frac{1}{r}\frac{\partial p_1}{\partial r} + \left(\beta_{n,1}^2 - \frac{n^2}{r^2}\right) p_1 = 0\,, \quad (2)$$

which is the Helmholtz equation expressed in cylindrical coordinates, assuming an effective wave number

$$\beta_{n,1} = \sqrt{\frac{-\left(4\Omega_1^2 + \zeta_{n,1}^2\right)}{c_1^2}}\,. \quad (3)$$

We verify that for $\Omega_1 = 0$, we recover the classical dispersion $\beta_1 = \omega/c_1$, with $c_1 = \sqrt{\kappa_1/\rho_1}$ the speed of sound inside the object (all parameters related to the object are denoted with subscript 1 and those related to free space with subscript 0). The behavior of $\beta_{n,1}$, i.e., the spinning effective wave number, is depicted in Figs. 1(b) and 1(c). As the parameter $\zeta_{n,1}$ is complex, $\beta_{n,1}$ possesses both imaginary and real parts (i.e., damping). For example, for $\beta_{0,1}$ (i.e., $n = 0$) in the domain $|\alpha_1| = |\Omega_1/\omega| \leqslant 1/2$, only the real part exists and decays exponentially, while reaching 0 for $\alpha_1 = \pm 1/2$. The imaginary part is zero in this domain and increases quasilinearly out of this domain. The orders $n = \pm 1$ possess similar and symmetric behavior. The orders $n = \pm 2$ have slightly different behavior, which is not symmetric with respect to α_1. It should be mentioned that for $\alpha_1 = 0$, i.e., no spinning, both wave numbers ($\beta_{n,1}$ and β_1) are equal, as expected. In the domain $|\alpha_1| \ll 1$, we should expect no damping of the spinning wave numbers, as observed.

Now, Eq. (2) shall be complemented with adequate boundary conditions. In the case of media at rest, we have continuity of the pressure field p_1 and the normal component of the velocity field (proportional to the displacement field) $v_{r,1} \propto p_1/\rho_1$. In the case of spinning media, we have continuity of the pressure and of the normal displacement $\psi_{r,1}$ [see Eq. (B5) in Appendix B] [80],

$$\begin{aligned} \psi_{r,1} &= \frac{\zeta_{n,1} v_{r,1} + \Omega_1 v_{\theta,1}}{\zeta_{n,1}^2 + \Omega_1^2} \\ &= \frac{\left(2\Omega_1^2 - \zeta_{n,1}^2\right)\partial_r p_1 - 3i\zeta_{n,1}\Omega_1 n p_1/r}{\rho_1\left(4\Omega_1^2 + \zeta_{n,1}^2\right)\left(\Omega_1^2 + \zeta_{n,1}^2\right)}\,. \end{aligned} \quad (4)$$

By letting $\Omega_1 = 0$ in Eq. (4), one gets a displacement proportional to $(1/\rho_1)\partial_r p_1$ as in the case for acoustic waves in media at rest.

B. Bessel expansion and scattering from bare spinning objects

Let us now turn to the main problem of characterizing the scattering from rotating cylindrical objects, at uniform angular velocity Ω_1. First we consider a bare cylindrical object of radius r_1 rotating in free space with density and bulk modulus ρ_1 and κ_1, respectively. At this stage, we will derive the general equation for any properties of the rotating object, and later, it will be assumed that $\rho_1 = \rho_0$ and $\kappa_1 = \kappa_0$ to single out the pure effects due to spinning. An acoustic plane wave of amplitude 1 is incident on the structure. For simplicity and without loss of generality, let us assume that the wave is in the x-y plane and that it propagates in the x direction. It can thus be expressed as $p^{\text{inc}} = e^{i\beta_0 x} = e^{i\beta_0 r\cos\theta}$, by ignoring the time-harmonic dependence, for now. The expansion of this incident plane wave in terms of Bessel functions takes the form

$$p^{\text{inc}} = \sum_{-\infty}^{+\infty} i^n J_n(\beta_0 r) e^{in\theta}\,. \quad (5)$$

The scattered field is expanded in terms of Hankel functions of the first kind to ensure that the Sommerfeld radiation condition is satisfied, i.e.,

$$p^{\text{scat}} = \sum_{-\infty}^{+\infty} i^n s_n H_n^{(1)}(\beta_0 r) e^{in\theta}\,, \quad (6)$$

for $r > r_1$ and with s_n the scattering coefficients to be determined using the boundary conditions at the interfaces of the structure. Hence, the field in region 0 is $p_0 = p^{\text{inc}} + p^{\text{scat}}$. These scattering coefficients intervene in the definition of the scattering amplitude $f(\theta) \propto \sqrt{r}\lim_{r\to\infty} p^{\text{scat}}(r,\theta)$, which is a measure of the acoustic scattering strength in the direction θ. The total scattering cross section (SCS) is the integration over all angles θ of the scattering amplitude and represents a scalar measure of the total scattering (irrespective of direction) and in the two-dimensional (2D) scenario is proportional to a length. For instance, we have

$$\sigma^{\text{scat}} = \frac{4}{\beta_0}\sum_{-\infty}^{+\infty} |s_n|^2\,. \quad (7)$$

To complete the expansion of the pressure fields, we consider now the case of the spinning disk of radius r_1 that is different from scattering objects that were considered in previous studies, so far. In this case and owing to the previous results, the pressure field in the region $r \leqslant r_1$ is given by

$$p_1 = \sum_{-\infty}^{+\infty} i^n a_n J_n(\beta_{n,1} r) e^{in\theta}\,, \quad (8)$$

with $\beta_{n,1}$ given in Eq. (3) and a_n unknown coefficients to be determined by the boundary conditions along with s_n. Now by equating the pressure and the displacement [see Eq. (4)] at the boundary $r = r_1$, we get

$$\begin{aligned} &p^{\text{inc}}(r_1) + p^{\text{scat}}(r_1) = p_1(r_1)\,, \\ &\frac{1}{\rho_0\omega^2}\frac{\partial\left(p^{\text{inc}} + p^{\text{scat}}\right)}{\partial r}\bigg|_{r=r_1} \\ &\quad = \frac{\left(2\Omega_1^2 - \zeta_{n,1}^2\right)\partial_r p_1 - 3i\zeta_{n,1}\Omega_1 n p_1/r}{\rho_1\left(4\Omega_1^2 + \zeta_{n,1}^2\right)\left(\Omega_1^2 + \zeta_{n,1}^2\right)}\bigg|_{r=r_1}\,. \end{aligned} \quad (9)$$

Equation (9) yields with the previous expansions a set of linear systems, for each azimuthal order n, thanks to the orthogonality of the functions $e^{in\theta}$, i.e.,

$$\begin{pmatrix} J_n(\beta_{n,1}r_1) & -H_n^{(1)}(\beta_0 r_1) \\ \Pi_{J_n} & -\frac{\beta_0}{\omega^2\rho_0}H_n^{(1)'}(\beta_0 r_1) \end{pmatrix}\begin{pmatrix} a_n \\ s_n \end{pmatrix} = \begin{pmatrix} J_n(\beta_0 r_1) \\ \frac{\beta_0}{\omega^2\rho_0}J_n'(\beta_0 r_1) \end{pmatrix}, \tag{10}$$

where the coefficient Π_{J_n} is expressed as

$$\Pi_{J_n} = \frac{\left(2\Omega_1^2 - \zeta_{n,1}^2\right)\beta_{n,1}J_n'(\beta_{n,1}r_1) - \frac{3\zeta_{n,1}\Omega_1 in}{r_1}J_n(\beta_{n,1}r_1)}{\rho_1\left(4\Omega_1^2 + \zeta_{n,1}^2\right)\left(\Omega_1^2 + \zeta_{n,1}^2\right)}. \tag{11}$$

Equation (11) shows clearly for the specific case of scattering from spinning objects that the multipoles of orders n and $-n$ give different contributions. The scattering coefficient s_n can be easily obtained from Eq. (10), i.e.,

$$s_n = \begin{vmatrix} J_n(\beta_{n,1}r_1) & J_n(\beta_0 r_1) \\ \Pi_{J_n} & \frac{\beta_0}{\omega^2\rho_0}J_n'(\beta_0 r_1) \end{vmatrix} \times \begin{vmatrix} J_n(\beta_{n,1}r_1) & -H_n^{(1)}(\beta_0 r_1) \\ \Pi_{J_n} & -\frac{\beta_0}{\omega^2\rho_0}H_n^{(1)'}(\beta_0 r_1) \end{vmatrix}^{-1}, \tag{12}$$

where $|M|$ denotes the determinant of a matrix M.

In order to single out the effect of rotation on the scattering, we consider an object with the same density and bulk modulus as the surrounding environment, i.e., $\rho_1 = \rho_0$ and $\kappa_1 = \kappa_0$. This leaves us with only the rotation angular velocity Ω_1 of the object ($r \leqslant r_1$). A scenario of interest is that of small objects compared to the sound wavelength, i.e., $\beta_0 r_1 \ll 1$ and $\beta_{n,1}r_1 \ll 1$. The first multipole terms are thus given by

$$\begin{aligned} s_0 &= \frac{3i\pi}{4}\frac{\alpha_1^2(\beta_1 r_1)^2}{1-\alpha_1^2} + O[(\beta_1 r_1)^4], \\ s_{\pm 1} &= \frac{i\pi}{4}\frac{\alpha_1(\beta_1 r_1)^2}{\pm 2 + \alpha_1} + O[(\beta_1 r_1)^4], \\ s_{\pm 2} &= \frac{i\pi}{32}\frac{\alpha_1(\beta_1 r_1)^4}{\mp 2 + \alpha_1} + O[(\beta_1 r_1)^6], \\ s_{\pm n} &= f_{\pm n}(\alpha_1)(\beta_1 r_1)^{2n} + O[(\beta_1 r_1)^{2n+2}]. \end{aligned} \tag{13}$$

In Eq. (13), $f_\pm$ denote functions of the variable α_1. The upper/lower signs in the second and third lines correspond to the positive/negative coefficient, respectively. Also, $O(\cdot)$ denotes the Landau notation (of a function of the same order) [81]. It may be noted that if the angular rotation velocity of the fluid goes to zero, all the scattering orders s_n vanish without exception. A case of interest is that of small rotation angular velocity, so the denominators in Eq. (13) are close to 1 and can be omitted; thus we have $s_0 \propto \alpha_1^2\omega^2$, $s_{\pm 1} \propto \alpha_1\omega^2$, and $s_{\pm 2} \propto \alpha_1\omega^4$. In classical scattering from nonrotating acoustic objects (or 2D electromagnetism), it is well known that the scattering cross section is dominated by both the zeroth order and first order, i.e., the monopole s_0 and the dipole s_1 [82]. However, from Eq. (13), we can see that $s_0/s_{\pm 1} \propto \alpha_1 \ll 1$ and $s_{\pm 2}/s_{\pm 1} \propto \omega^2 \ll 1$. Hence, unlike for the case of acoustics at rest [77], the SCS of spinning objects is dominated by the dipole terms $s_{\pm 1}$. The higher-order terms scale as $(\beta_1 r_1)^{2n}$ and do not contribute significantly to the scattering, although in Eq. (11) we have terms proportional to n. However, the peculiar behavior of Bessel functions makes the higher-order multipoles negligible in the quasistatic limit.

Another interesting remark about scattering of spinning fluids can be immediately seen upon inspection of Eq. (13). We can see that the scattering coefficients possess poles for determined values of α_1. Namely, these are $\omega = \pm\Omega_1$ for s_0, $\mp\Omega_1/2$ for $s_{1,-1}$, and $\pm\Omega_1/2$ for $s_{2,-2}$. Thus for these frequencies, resonant scattering may be observed. For instance,

$$\sigma^{\text{scat}} \approx (\beta_0 r_1)^3 \frac{\alpha_1^2\left(\alpha_1^2+4\right)}{\left(\alpha_1^2-4\right)^2}. \tag{14}$$

Figure 2(a) plots these normalized scattering coefficients $4/\beta_0|s_n|^2$ in logarithmic scale versus frequency (in logarithmic scale, too) for a spinning object (made of water, as the surrounding, and separated from it by a thin membrane), with $\Omega_1 = 2\pi$ rad/s, of radius $r_1 = 1$ m, bulk modulus and density $\kappa_1 = \kappa_0 = 2.22$ GPa and $\rho_1 = \rho_0 = 10^3$ kg/m^3, respectively, for $n = 0, \pm 1, \pm 2$. These plots show that although the object has the same physical parameters as the environment (water, here, for instance), resonant modes take place at specific frequencies given by Eq. (13). It should be also noted that both modes $n = 0$ and $n = \pm 1$ dominate, as can be anticipated from Eq. (13). Also the resonance of modes $n = 1$ and $n = -2$ cannot be seen here as we use positive $\Omega_1 (= 2\pi$ rad/s). Figure 2(b) depicts the total scattering cross section σ_{scat} with 21 scattering orders taken into account ($n = -10 : 10$) versus the normalized spinning velocity for different kinds of objects, ranging from soft, i.e., $\sqrt{(\kappa_1\rho_1)/(\kappa_0\rho_0)} \ll 1$ [green line in Fig. 2(b)], to "nonrigid," i.e., $\sqrt{(\kappa_1\rho_1)/(\kappa_0\rho_0)} \approx 1$ [red and blue lines in Fig. 2(b)], to hard wall (rigid) (detailed in Sec. III C), i.e., $\sqrt{(\kappa_1\rho_1)/(\kappa_0\rho_0)} \gg 1$ [black dashed line in Fig. 2(b)]. The resonant scattering can be seen from all these objects around the predicted spinning velocities. Here the frequency is fixed at 1 Hz (quasistatic limit). It should be noted that the presence of these Mie resonances is unusual in acoustics, where homogeneous objects do not possess low-frequency resonance. The only case of low-frequency Mie resonances concerns flexural waves scattered off thin-plate objects as was analyzed in Ref. [83], originating from the peculiar nature of flexural biharmonic waves obeying a fourth-order PDE [84]. However, in the present scenario, these resonances are due to pure rotation. Figure 2(c) plots contours of normalized SCS σ^{scat}/r_1 (in logarithmic scale) of a scatterer with the same physical properties as the surroundings (water) for varying frequencies ω and spinning speeds Ω_1. This plot clearly shows that the SCS has two resonances (marked with dark red color) for each spinning speed. Moreover, the blue horizontal thick linear region at the center with blue color (i.e., zero scattering) corresponds to very low, down to zero spinning speeds, and as the scatterer possesses the same density and bulk modulus as the surrounding, it does not scatter at all at these low spinning speeds. On the other hand, if we take vertical cuts along this 2D graph, four resonances occur (in a symmetric manner with respect to Ω_1) as it transpires from Fig. 2(b) and as predicted from Eq. (13).

The inset of Fig. 2(c) plots the real part distribution of the pressure field [$\Re(p)$] in the scattering region (i.e., region 0) in the presence of the spinning acoustic cylinder. These plots correspond to frequencies and spinning speeds of different resonating modes, as depicted in Fig. 2(c). It may be seen

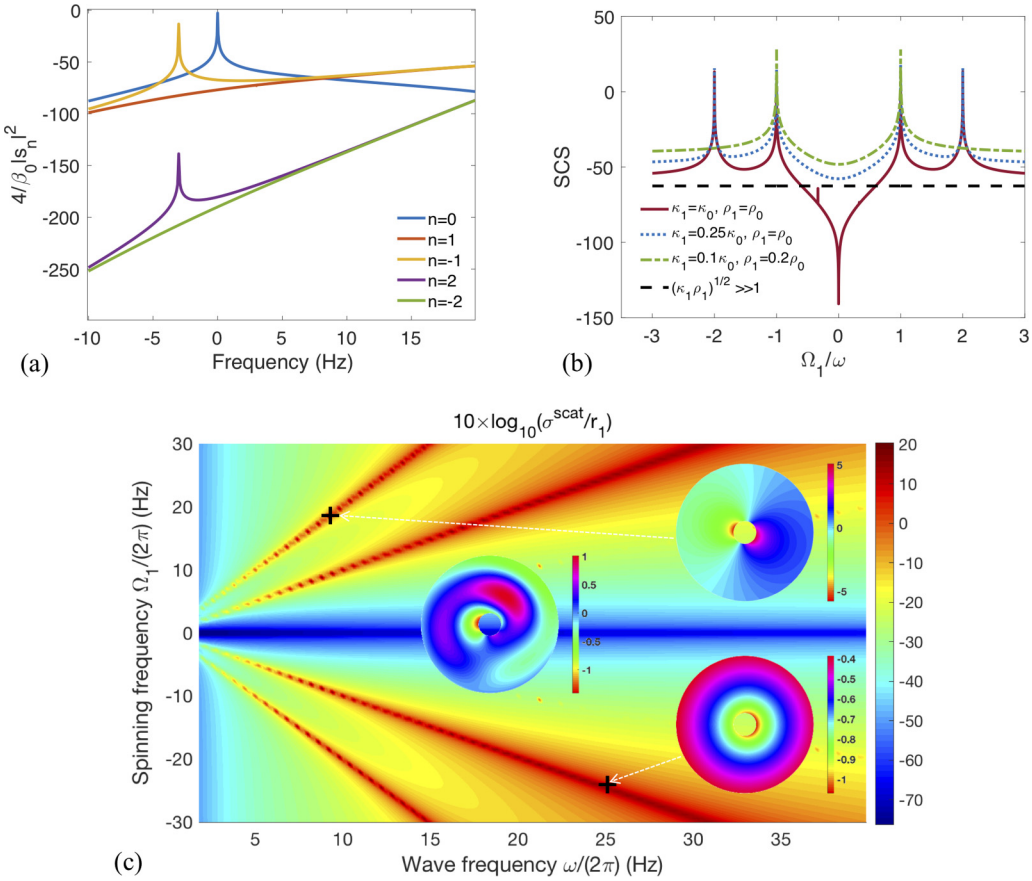

FIG. 2. (a) Scattering coefficients $4/\beta_0|s_n|^2$ in logarithmic scale vs frequency (in logarithmic scale, too) for a spinning object [$\Omega_1/(2\pi) = 1$ Hz] of radius $r_1 = 1$ m, bulk modulus and density $\kappa_1 = \kappa_0 = 2.22$ GPa and $\rho_1 = \rho_0 = 10^3 \mathrm{kg/m^3}$, respectively, for $n = 0, \pm1, \pm2$. (b) Total normalized SCS ($\sigma^{\mathrm{scat}}/r_1$) with 21 scattering orders taken into account ($n = -10, -9, \ldots, 10$) vs the normalized spinning velocity for different kinds of objects, ranging from soft ($\sqrt{\kappa_1\rho_1} \ll 1$), "normal" ($\sqrt{\kappa_1\rho_1} \approx 1$), to hard wall (see Sec. III C) ($\sqrt{\kappa_1\rho_1} \gg 1$). (c) Normalized SCS, in logarithmic scale, of the spinning cylinder vs the frequency of the acoustic wave ω and the spinning velocity Ω_1 for the same physical parameters as the environment (water). The inset plots $\Re(p_0)$ at corresponding parameters. The middle one corresponds to a high frequency, $\Omega_1 = 2\omega = 2\pi \times 500$ Hz.

that the pressure field takes very large values (in comparison to the nonresonating case, where $\Re(p) \approx 10^{-3}p_0$), which is coherent with the observed Mie resonance due to the spinning fluid.

III. SCATTERING CANCELLATION FOR SPINNING CYLINDERS

A. Bessel function expansion for the core-shell structure

Let us now turn to the analysis of cloaking the spinning objects using the paradigm of the scattering cancellation technique [52]. We consider a core-shell structure, depicted in Fig. 1(a), with an object of radius r_1 and a shell of radius r_2. The parameters of the object and the shell are denoted by $\rho_{1,2}$, $\kappa_{1,2}$, and $\Omega_{1,2}$, for the density, bulk modulus, and angular velocity, respectively. On the other side, the parameters of free space are just ρ_0 and κ_0, as the fluid in region 0 is at rest. The field expansions are similar to those of a bare object. However, we have now an additional domain (the shell) $r_1 < r \leqslant r_2$, within which the pressure field can be expanded as

$$p_2 = \sum_{-\infty}^{+\infty} i^n [b_n J_n(\beta_{n,2} r) + c_n Y_n(\beta_{n,2} r)] e^{in\theta}, \qquad (15)$$

with Y_n the Bessel function of the second kind, $\beta_{n,2} = \sqrt{-(4\Omega_2^2 + \xi_{n,2}^2)/c_2^2}$ and $c_2 = \sqrt{\kappa_2/\rho_2}$.

The obtained scattering system for this structure is thus obtained by applying the same boundary conditions at the interfaces $r = r_1$ and $r = r_2$, taking into account that the fluid is either rotating or at rest. This leads to

$$\begin{pmatrix} 0 & J_n(\beta_{n,2}r_2) & Y_n(\beta_{n,2}r_2) & -H_n^{(1)}(\beta_0 r_2) \\ 0 & \Pi_{J_n}(\beta_{n,2}r_2) & \Pi_{Y_n}(\beta_{n,2}r_2) & -\frac{\beta_0}{\omega^2\rho_0} H_n^{(1)'}(\beta_0 r_2) \\ -J_n(\beta_{n,1}r_1) & J_n(\beta_{n,2}r_1) & Y_n(\beta_{n,2}r_1) & 0 \\ -\Pi_{J_n}(\beta_{n,1}r_1) & \Pi_{J_n}(\beta_{n,2}r_1) & \Pi_{Y_n}(\beta_{n,2}r_1) & 0 \end{pmatrix} \begin{pmatrix} a_n \\ b_n \\ c_n \\ s_n \end{pmatrix} = \begin{pmatrix} J_n(\beta_0 r_2) \\ \frac{\beta_0}{\omega^2\rho_0} J_n'(\beta_0 r_2) \\ 0 \\ 0 \end{pmatrix}, \qquad (16)$$

with the functionals Π_{Y_n} given in the same way as Π_{J_n}, shown in Eq. (11), up to the replacement of J_n by Y_n. The scattering coefficient is thus $s_n = |M|/|\tilde{M}|$, where M is the 4×4 matrix in the left-hand side of Eq. (16), and $\tilde{M}$ is the matrix obtained from M by replacing its fourth column vector by the vector in the right-hand side of Eq. (16). Solving Eq. (16) is straightforward using a numerical software such as MATLAB [85], and this will be performed later to characterize and analyze this peculiar cloaking mechanism.

B. Analysis of the SCT

In order to gain more insight and due to the general complexity of this linear system, it is instructive to analyze the long-wavelength limit (as done for the bare object in previous section) corresponding to acoustically small objects and shells, i.e., $\beta_0 r_j \ll 1$ and $\beta_{n,j} r_j \ll 1$, where $j = 1, 2$. Note that with the values of the parameters in this study, it is sufficient to impose the first condition $\beta_0 r_1 \ll 1$. Under these assumptions and by denoting $\Omega_1 = \alpha_1 \omega$, $\Omega_2 = \alpha_2 \omega$, $r_2 = r_1/\gamma$, and by choosing without loss of generality $\rho_2 = \rho_1 = \rho_0$ and $c_2 = c_1 = c_0$ in order to single out the effect of spinning (by ignoring scattering due to the acoustic impedance mismatch due to inhomogeneities), we obtain for the leading scattering orders, as discussed in the previous section,

$$s_0 = \frac{3i\pi}{4\gamma^2} \frac{\left[\gamma^2\alpha_1^2 - \left(-1 + \gamma^2 + \alpha_1^2\right)\alpha_1\alpha_2\right]}{\left(-1 + \alpha_1^2\right)(-1 + \alpha_1\alpha_2)} (\beta_0 r_1)^2 + O[(\beta_0 r_1)^4] \tag{17}$$

and

$$s_{\pm 1} = \frac{i\pi}{4\gamma^2} \frac{A_{\pm 1}}{B_{\pm 1}} (\beta_0 r_1)^2 + O[(\beta_0 r_1)^3], \tag{18}$$

with

$$A_{\pm 1} = \pm 2\gamma^2\alpha_1 + \alpha_2(\pm 2 \mp 2\gamma^2 + \alpha_1 - 6\gamma^2\alpha_1) + \alpha_2^2(-3 + 6\gamma^2 \pm \alpha_1 \pm 4\gamma^2\alpha_1) + \alpha_2^3(\pm 1 \mp 4\gamma^2 + 6\gamma^2\alpha_1) + \alpha_2^4[6(1 - \gamma^2)] \tag{19}$$

and

$$B_{\pm 1} = 4 \pm 2\alpha_1 + \alpha_2(\mp 4 + 3\alpha_1 - 2\gamma^2\alpha_1) + \alpha_2^2(-1 + 2\gamma^2 \pm \alpha_1 \mp 2\gamma^2\alpha_1) + \alpha_2^3(\pm 13 \pm 2\gamma^2 + 6\gamma^2\alpha_1) + \alpha_2^4[6(1 - \gamma^2)]. \tag{20}$$

In Eqs. (19) and (20) the upper (lower) signs correspond to the order $n = 1$ ($n = -1$). Note that as $\alpha_2 \to 0$, i.e., the shell is at rest, the expressions of s_0 and $s_{\pm 1}$ given in Eqs. (17)–(20) reduce to those given in Eq. (13), as would be expected.

In order to cancel the total SCS, i.e., σ^{scat}, we have to enforce simultaneously $s_0 = 0$ and $s_{\pm 1} = 0$. For small angular rotation speeds, only $s_{\pm 1}$ is significant [as we have seen earlier from Eq. (13)], and it is safe to ignore the contribution of the higher-order multipoles ($|n| \geqslant 2$), as these scale with $(\beta_0 r_1)^{2n}$ [their squared amplitude, i.e., their contribution to the SCS, from Eq. (7), scales with $(\beta_0 r_1)^{4n-1}$, which is even smaller].

First, enforcing $|s_0| = 0$, we derive the quasistatic condition of SCT, i.e.,

$$\gamma^2\alpha_1^2 - \left(-1 + \gamma^2 + \alpha_1^2\right)\alpha_2^2 = 0, \tag{21}$$

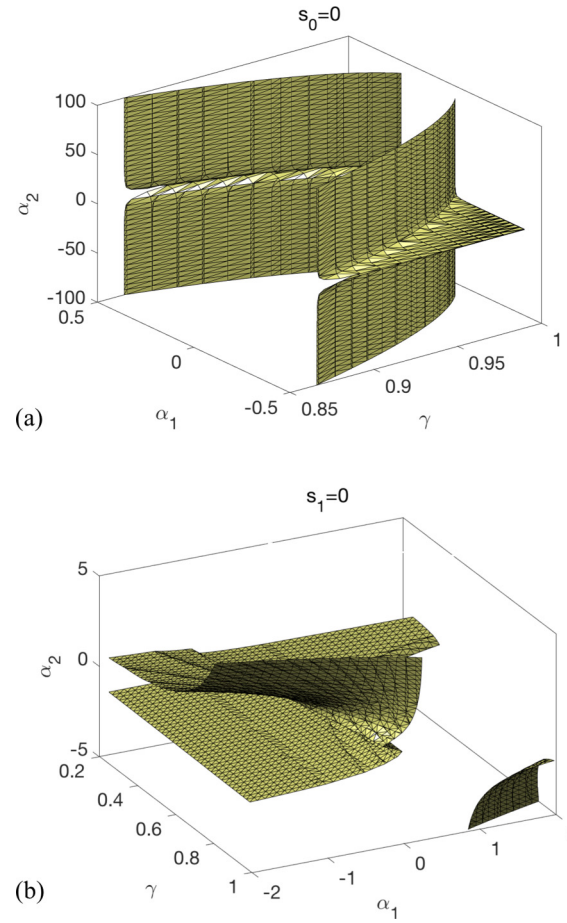

FIG. 3. (a) Contour plot of α_2 vs α_1 and γ for the first-order ($n = 0$) condition, given in Eq. (17). (b) Contour plot of α_2 vs α_1 and γ for the second-order condition ($n = \pm 1$), given in Eqs. (18)–(20).

which relates α_2, α_1, r_1, and r_2 (via γ). It is found that to satisfy Eq. (20), α_2 must take positive and/or negative values. Note that positive (resp. negative) angular velocity just means an anticlockwise (resp. clockwise) rotation. We thus have

$$\alpha_2 = \pm \frac{\gamma\alpha_1}{\sqrt{\left(-1 + \gamma^2 + \alpha_1^2\right)}}. \tag{22}$$

Also, when $\gamma^2 + \alpha_1^2 \leqslant 1$, no solution can be found that may cancel the scattering monopole s_0. The behavior of α_2, versus γ and α_1, corresponding to Eq. (17) is depicted in Fig. 3(a) [see Fig. 8 for a different view of the same plot]. Specifically, we can observe that for the domain $\gamma^2 + \alpha_1^2 \leqslant 1$, no solution for α_2 can be found (empty region of the plot). For $\gamma^2 + \alpha_1^2 = 1$, very high positive (and negative) values of α_2 are required. On the other hand, when the condition on $\gamma^2 + \alpha_1^2$ is relaxed, small values of α_2 are sufficient. It should also be noted that α_2 is symmetric with respect to the variation of α_1 (α_1 and $-\alpha_1$ give the same values of α_2), as seen from Fig. 3(a).

Let us now turn to the analysis of canceling the leading scattering dipole orders $s_{\pm 1}$. In fact, Eq. (19) is of fourth order, so we may expect to obtain four distinct solutions for α_2. This is exactly what may be observed in Fig. 3(b), where four branches can be distinguished in this three-dimensional contour plot. In this scenario, we can see that there is a lack

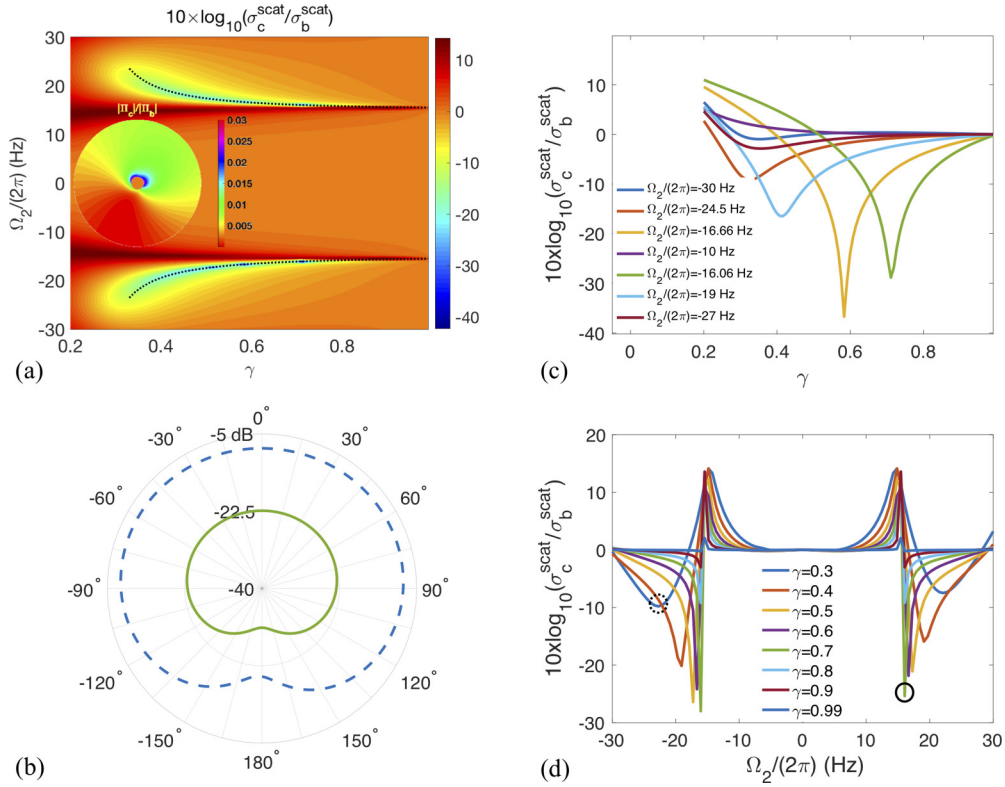

FIG. 4. (a) Normalized SCS ($\sigma_c^{\text{scat}}/\sigma_b^{\text{scat}}$) in logarithmic scale (where the subscripts b and c refer to the scattering cross section of the obstacle and cloaked structure, respectively) vs the spinning frequency of the cloaking shell $\Omega_2/(2\pi)$ and the radii ratio γ. The bright regions represent the locations of optimized scattering reduction, with values exceeding 40 dB (in absolute value). The inset gives the acoustic Poynting vector of the cloaked structure normalized by that of the bare object in the scattering region. (b) Scattering amplitude ($|f(\theta)|^2$) in logarithmic scale for the cloaked structure (normalized by the amplitude of the bare object) for $\Omega_2/(2\pi) = 16.06$ Hz (solid line, clockwise motion) and $\Omega_2/(2\pi) = -22.7$ Hz (dashed line, anticlockwise motion) corresponding to the highlighted values from (d). (c) Normalized SCS vs γ for various values of $\Omega_2/(2\pi)$. (c) Normalized SCS vs the spinning frequency of the cloaking shell $\Omega_2/(2\pi)$ for various values of γ. All these figures were plotted for a frequency of $\omega/(2\pi) = 15.5$ Hz and $\Omega_1/(2\pi) = 15$ Hz.

of symmetry with respect to α_1 due to the presence of the dipole order term in the equation ($n = \pm 1$). Clockwise and anticlockwise rotations Ω_2 are thus viable ways to counteract the anticlockwise rotation of the object and make it look static to external observers (by canceling the $n = \pm 1$ multipoles). The angular rotation speeds needed here are also comparable to the speed of the object to cancel. The graphs of Fig. 3 are only dependent on frequency through the parameters $\alpha_i = \Omega_i/\omega$.

Next, we consider the general case where we do not make use of the asymptotic (quasistatic) approximation and solve the exact scattering problem, stemming from Eq. (16). The angular rotation speed of the fluid in region 1 ($r \leqslant r_1$) is $\Omega_1/(2\pi) = 15$ Hz, and its density and bulk modulus are assumed, as before, equal to those of free space (water). Here, the frequency of the wave is chosen as $\omega/(2\pi) = 15.5$ Hz (high spinning regime, i.e., $\Omega_1 \approx \omega$). σ_c^{scat} of the total object-shell structure is normalized with the SCS of the bare object and subsequently plotted against varying values of $\Omega_2/(2\pi)$ and γ. This result is shown in Fig. 4(a) in logarithmic scale. The regions colored with dark blue correspond to significant scattering reduction (i.e., $\sigma_c^{\text{scat}}/\sigma_b^{\text{scat}} \ll 1$), whereas the dark red regions correspond to enhanced scattering from the core-shell geometry. It can be seen that two distinct regions of cloaking can be distinguished, i.e., for $\Omega_2/(2\pi) > 15.5$ Hz and for $\Omega_2/(2\pi) < -15.5$ Hz, and both with values of γ between 0.4 and 0.8, for efficient scattering reduction. In particular, a minimum of -40 dB of $\sigma_c^{\text{scat}}/\sigma_b^{\text{scat}} \ll 1$ is seen around values of $\Omega_2/(2\pi) = -16.7$ Hz and $\gamma = 0.6$. In addition, the dashed black lines give the results of Eqs. (17) and (22).

To isolate the effect of Ω_2 and γ on the scattering reduction mechanism, a plot of $\sigma_c^{\text{scat}}/\sigma_b^{\text{scat}}$ is given versus γ and for different values of $\Omega_2/(2\pi)$. We can see in Fig. 4(c) that one single cloaking regime takes place. For higher values (in absolute value) of $\Omega_2/(2\pi)$ the cloaking is broader with γ but less pronounced. When $\Omega_2/(2\pi)$ approaches ± 15.5 Hz, the scattering reduction is higher but less broad with respect to γ. In addition, for the frequency range $\Omega_2/(2\pi) \in [-15.5, 15.5]$ Hz, no cloaking can take place. Next, $\sigma_c^{\text{scat}}/\sigma_b^{\text{scat}} \ll 1$ is given versus $\Omega_2/(2\pi)$ for different values of γ in Fig. 4(d). We can see that two scattering dips exist for different values of γ. For instance, for $\gamma < 0.4$ and $\gamma > 0.8$, no cloaking is possible. The minimum cloaking is for $\Omega_2 = -16.7$ Hz and $\gamma = 0.6$. To better illustrate the efficiency of the proposed cloak, the far-field scattering patterns (i.e., $|f(\theta)|$) in polar coordinates are shown in Fig. 4(b) for two specific parameters of Ω_2 and γ, depicted in Fig. 4(d) with circles. This plot demonstrates that the spinning fluid is undetectable for all angles [Fig. 4(c) gives normalized $|f_c(\theta)/f_b(\theta)|$, with subscripts c and b denoting,

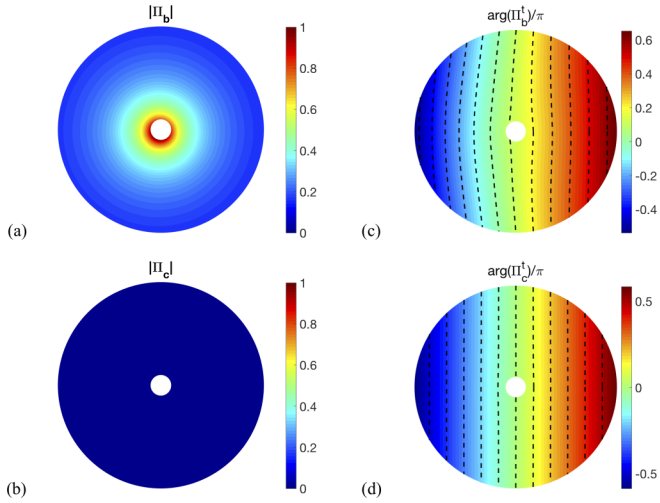

FIG. 5. (a) Near-field plot (in arbitrary units) of the acoustic scattered Poynting vector $\mathbf{\Pi}_b$ (proportional to $|p^{\text{scat}}|^2$) of the bare object of radius $r_1 = 1$ m, spinning with speed $\Omega_1/(2\pi) = 15$ Hz at the frequency $\omega/(2\pi) = 15.5$ Hz. (b) Same as in (a) for the cloaked object ($\mathbf{\Pi}_c$), with the shell of radius $r_2 = r_1/\gamma$ and $\gamma = 0.71$ and spinning frequency $\Omega_2/(2\pi) = -16$ Hz. The physical parameters of the object and shell are equal to those of the surrounding, i.e., water. The phases (normalized with π) of the total Poynting vectors are given in (c) and (d) for the bare and cloaked object with same parameters as in (a) and (b), respectively. The black dashed lines represent the contours of the phases.

as before, the cloaked and bare object, respectively]. In fact, it should be understood that the continuous line offers better cloaking than the dashed one, which is translated by a smaller SCS (which is clearly visible in the figure.) However, it can be remarked that the scattering amplitude is reduced more for some angles (180°, for instance). Hence, for the continuous curve, the scattering reduction ranges from −23 to −35 dB, which is considered as being cloaking for all angles. For the dashed curve, the scattering reduction is not very efficient and it is around 10 dB, on average. This is visible in Fig. 4(d), which gives the SCS (which is the integration of the scattering amplitude over all angles and is a better measure of scattering reduction). This plot confirms that a clockwise rotating shell of small radius can cloak an anticlockwise spinning object.

Last, Figs. 5(a) and 5(b) plot the near-field scattered pressure field amplitude (or more precisely, the amplitude of the normalized scattered acoustic Poynting vector [86], i.e., $|\mathbf{\Pi}_b|$ and $/|\mathbf{\Pi}_c|$) in the environment region (region 0) for the bare object and cloaked object, respectively. We can observe that a drastic reduction of the scattered fields (about two orders of magnitude) takes place in the case of an object with spinning coating. The phases (normalized with π) of the total Poynting vectors are given in Figs. 5(c) and 5(d) for the bare and cloaked object with same parameters as in Figs. 5(a) and 5(b), respectively. These plots show that the phase of the fields is not distorted in the case of a cloaked scenario (straight parallel contour lines, marked with the dashed black lines), whereas for the bare case it is slightly distorted (contour lines are curved due to the enhanced scattering from the spinning object). A discussion on the frequency response of the cloaking mechanism and near-fields at a different frequency are given in Appendix A, Fig. 9.

C. The case of a hard-wall object

Let us now first derive the equivalence of the scattering from a hard-wall object and an infinite acoustic impedance object [different from the case of a finite acoustic inhomogeneity, shown for comparison in Fig. 6(a)]. The hard-wall (rigid) boundary condition is for $r = r_1$, namely, $\mathbf{n} \cdot \mathbf{v} = 0$ (or in terms of pressure $1/\rho\, \partial_r p = 0$). The incident field is as usual a plane-wave expressed as in Eq. (5) and the scattered pressure is given as in Eq. (6). By application of the hard-wall boundary condition at r_1, we obtain the expression of the coefficients,

$$s_n^{(r)} = \frac{-J_n'(\beta_0 r_1)}{H_n^{(1)'}(\beta_0 r_1)}, \quad \forall n \in \mathbb{Z}\,. \tag{23}$$

On the other hand, an object of same radius r_1, density ρ_1, and bulk modulus κ_1 embedded in a homogeneous medium of density ρ_0 and bulk modulus κ_0 possesses scattering given by

$$s_n = \begin{vmatrix} J_n(\beta_1 r_1) & J_n(\beta_0 r_1) \\ J_n'(\beta_1 r_1) & \chi J_n'(\beta_0 r_1) \end{vmatrix} \begin{vmatrix} J_n(\beta_1 r_1) & H_n^{(1)}(\beta_0 r_1) \\ J_n'(\beta_1 r_1) & \chi H_n^{(1)'}(\beta_0 r_1) \end{vmatrix}^{-1}, \tag{24}$$

where $\chi = Z_1/Z_0$, and $Z_{0,1} = \sqrt{\rho_{0,1}\kappa_{0,1}}$ is the impedance of the object and free space, respectively.

Now, in order to establish the analogy between the hard-wall boundary and the inhomogeneous medium, we must equalize Eqs. (23) and (24). This can be obtained for all scattering orders if we ensure that $\chi \to \infty$, i.e., by assuming an infinite impedance of the object. This is somehow coherent, as the higher impedance leads to enhanced reflection, and in this limit the fields cannot penetrate the object, which is an equivalent to a hard-wall boundary. This fact is demonstrated in Fig. 6(b), where the plot of the SCS versus a broadband of frequencies is depicted. It can be also seen from Fig. 6(b) that rotating a hard-wall object does not change its scattering response, unlike for the case of an acoustic medium with finite impedance, shown in Fig. 6(a). This is mainly because there is no flow inside the object (pressure and velocity are zero for $r < r_1$), and hence rotating the object does not induce any extra scattering features.

Last, to verify the versatility and robustness of this new kind of SCT-based cloaking, we investigate the possibility to cloak a rigid (hard-wall-like) cylindrical object by using only a rotating shell of the same physical parameters (ρ_2 and κ_2) as those of the surrounding medium (water, here). The rigid body can mimic, for example, a submarine, or any underwater solid (we ignore shear waves here, as only compression waves are investigated). We first coat the rigid object of radius $r_1 = 1$ m with a shell of radius $r_2 = 1.2$ m, and we sweep the density and bulk modulus of the shell, as usually done in SCT cloaking. The normalized SCS is plotted as before, at frequency $\omega/(2\pi) = 383$ Hz, and the result is depicted in Fig. 6(c). On the other hand, we consider coating the same object with a shell of radius $r_2 = r_1/\gamma$ and spinning angular frequency Ω_2. In this scenario $\rho_2 = \rho_0$ and $\kappa_2 = \kappa_0$. So the SCT is induced here purely by the spinning effect. The result is depicted in Fig. 6(d), and it can be clearly seen that comparable scattering cancellation is possible to achieve. The

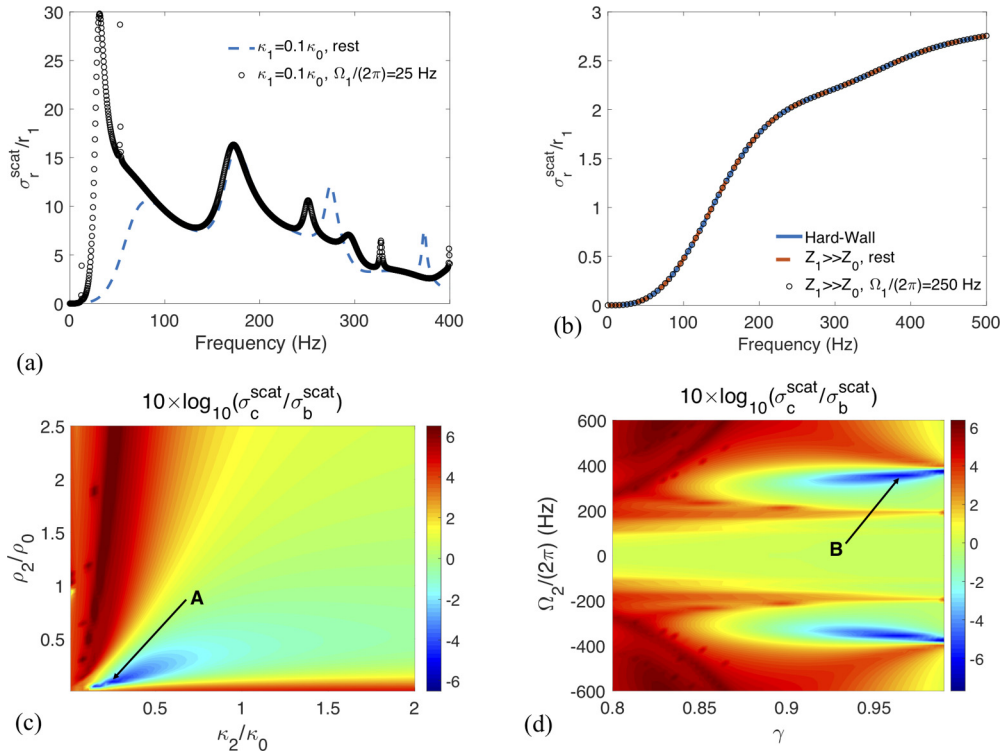

FIG. 6. (a) SCS for an object of radius 1 m, density $\rho_1 = \rho_0$, bulk modulus $\kappa_1 = 0.1 \times \kappa_0$ vs frequency when the object is at rest (dashed blue curve) and when it is spinning with $\Omega_1/(2\pi) = 25$ Hz (black circles). (b) SCS for the hard-wall boundary (blue line), infinite acoustic impedance approximation, i.e., $\sqrt{\rho_1\kappa_1} \to \infty$ (red dashed line), and spinning infinite acoustic impedance approximation (circles). (c) Cloaking scenario for the hard-wall object of radius $r_1 = 1$ m when using classical SCT scheme, i.e., by varying the density and bulk modulus of the shell of radius $r_2 = 1.2$ m at frequency $\omega/(2\pi) = 383$ Hz. (d) Same as in (c) but using a spinning shell of density and bulk modulus equal to those of free space.

advantage is here that we do not need near-zero or negative density and/or bulk modulus for the cloaking operation [as can be seen from Fig. 6(c)]. By pure rotation of homogeneous shells, cloaking is made possible. Note that we can further improve this scattering cancellation with spinning by allowing some freedom for the density and/or bulk modulus of the shell.

Figure 7 plots the phases (normalized with π) of the total Poynting vectors for the bare and cloaked object, corresponding to points A and B, highlighted in Figs. 6(c) and 6(d). These plots show that the phase of the fields is not distorted in the case of a cloaked scenario (straight contour lines, marked with the dashed black lines), whereas for the bare case it is slightly distorted (contour lines are curved due to the enhanced scattering from the spinning object). This plot also confirms the findings of Figs. 6(c) and 6(d).

Figure 7(a) depicts the phase of the total Poynting vector of a bare rigid object of radius unity at frequency $\omega/(2\pi) = 383$ Hz, whereas Fig. 7(b) gives the same quantity for the rigid object at frequency $\omega/(2\pi) = 383$ Hz, cloaked by a shell of radius 1.2 m, density and bulk modulus corresponding to point A in Fig. 6(c), i.e., $\rho_2 = 0.094\rho_0$ and $\kappa_2 = 0.246\kappa_0$. Next, Figs. 7(c) and 7(d) give the same situation, but here $\rho_2 = \rho_0$ and $\kappa_2 = \kappa_0$; however, $\Omega_2/(2\pi) = -366$ Hz and $\gamma = 0.958$, corresponding to point B in Fig. 6(d). Both scenarios show comparable scattering reduction, thus demonstrating the efficiency of spinning shells in cloaking rigid objects.

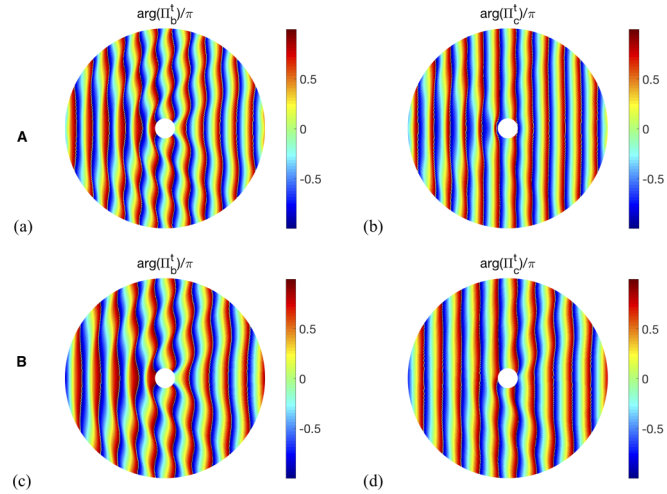

FIG. 7. (a) Phase (normalized with π) of the total Poynting vectors of a bare rigid object of radius unity at frequency $\omega/(2\pi) = 383$ Hz. (b) Phase (normalized with π) of the total Poynting vectors of a rigid object of radius unity at frequency $\omega/(2\pi) = 383$ Hz, cloaked by a shell of radius 1.2 m, density and bulk modulus corresponding to point A in Fig. 6(c), i.e., $\rho_2 = 0.094\rho_0$ and $\kappa_2 = 0.246\kappa_0$. (c) Same as in (a). (d) Same as in (b) but here $\rho_2 = \rho_0$ and $\kappa_2 = \kappa_0$; however, $\Omega_2/(2\pi) = -366$ Hz and $\gamma = 0.958$, corresponding to point B in Fig. 6(d).

IV. CONCLUDING REMARKS

In summary, a detailed analysis of spinning acoustic objects and their scattering properties is proposed, and acoustic cloaks based on the scattering cancellation technique are designed. Here the main challenge is that the object to conceal (cloak) is not at rest and experiences rotation along its z axis (for cylinders) at constant angular speed (with a few rotation cycles per second). Scattering by such acoustic rotating objects is physically different from objects at rest and possesses resonant Mie features at specific frequencies. The cloaking mechanism introduced here presents several advantages in comparison with zero-velocity cloaking, as it may be more useful in realistic applications (where objects are most of the time moving). Using a homogeneous layer of the same properties as free space with a rotation (in the opposite direction to the object), we are able to significantly reduce the scattering from objects with various spinning speeds. It is also shown that using purely a spinning shell, it is possible to cancel the scattering from a rigid (hard-wall) object in a similar manner as optimizing its density and bulk modulus, which shows the versatility of this cloaking mechanism.

Experimental realization of this concept may be within reach readily, as it only requires rotating objects and shells, allowing for interesting applications in scenarios in which it is desirable to suppress the scattering from obstacles that are in a spinning movement (e.g., rotating components of cars or helicopter rotor blades) for noise reduction. The same concept can also be generalized to other classes of waves, such as linear surface water waves, flexural waves in thin plates, or beams.

ACKNOWLEDGMENT

The research reported in this manuscript was supported by King Abdullah University of Science and Technology Baseline Research Fund BAS/1/1626-01-01. A.A. acknowledges support from the Air Force Office of Scientific Research.

APPENDIX A: CHARACTERIZATION OF THE SCT CLOAKING

To give a better view of the analytical results of Fig. 3, Fig. 8 plots the same results but from a different view angle. In order to characterize the efficiency of the cloaking mechanism presented in this work, Fig. 9 gives the scattering response versus frequency. For instance, Fig. 9 plots the normalized SCS ($\sigma_c^{\text{scat}}/\sigma_b^{\text{scat}}$) in logarithmic scale (where the subscripts b and c refer to the SCS of the bare obstacle and cloaked one, respectively) versus the wave frequency $\omega/(2\pi)$ and the spinning frequency of the cloaking shell $\Omega_2/(2\pi)$, for $\gamma = 0.71$ and an object of radius 1 m and spinning frequency $\Omega_1/(2\pi) = 15$ Hz, and the same physical parameters as the surrounding, for both object and cloaking shell. The dark blue regions represent the locations of optimized scattering reduction, with values exceeding 30 dB (in absolute value). This figure shows also that two cloaking peaks can be attained, the first one around frequency 7.5 Hz, which is hardly tunable, whereas the second one can be controlled by varying the spinning frequency of the cloaking shell. This is shown more clearly in Fig. 9(c), which gives the normalized SCS versus wave frequency $\omega/(2\pi)$ for various values of $\Omega_2/(2\pi)$,

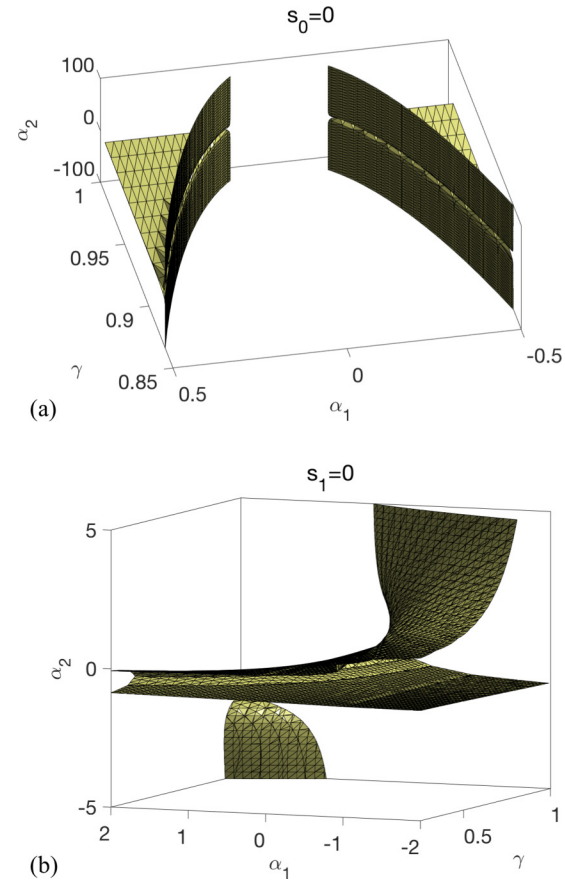

FIG. 8. Same as in Fig. 3 but with a rotated view to highlight the different solutions of Eqs. (17)–(20).

corresponding to the dashed colored lines in Fig. 9(a). The phase (normalized with π) of the total Poynting vector for the cloaked object corresponding to the situation encircled in Fig. 9(c) is given in Fig. 9(d) along with the contours of the phases (black dashed lines). Moreover, in this scenario, we wished to isolate the pure effects of scattering and scattering cancellation due solely to spinning by assuming $\rho_{1,2} = \rho_0$ and $\kappa_{1,2} = \kappa_0$. However, another interesting case is to consider an object of $\rho_1 \neq \rho_0$ and $\kappa_1 \neq \kappa_0$. This scenario is plotted in Fig. 9(b), where an object has $\rho_1 = \rho_0$ but $\kappa_1 = 0.1 \times \kappa_0$ and moderate spinning $\Omega_1/(2\pi) = 5$ Hz. The shell has also the same radius as in Fig. 9(a), $\rho_2 = \rho_0$, but $\kappa_2 = -0.11 \times \kappa_0$. This 2D plot shows that broadband scattering reduction can be achieved for a large interval of spinning frequencies of the shell. A particular scenario is plotted by the dashed curve which corresponds to a specific $\Omega_2/(2\pi) = -5$ Hz, and its axis is shown. From this plot we can see that for most of the frequency domain considered here, a scattering reduction of at least 20 dB can be achieved, which shows that this technique is efficient to cloak acoustic inhomogeneities with spinning movement, by tailoring the shell's physical properties.

APPENDIX B: DERIVATION OF THE ACOUSTIC EQUATION IN SPINNING MEDIA

Let us consider a uniformly rotating medium as schematized in Fig. 1(a). The usual equations of motion (momentum conservation) and continuity (conservation of mass) need to

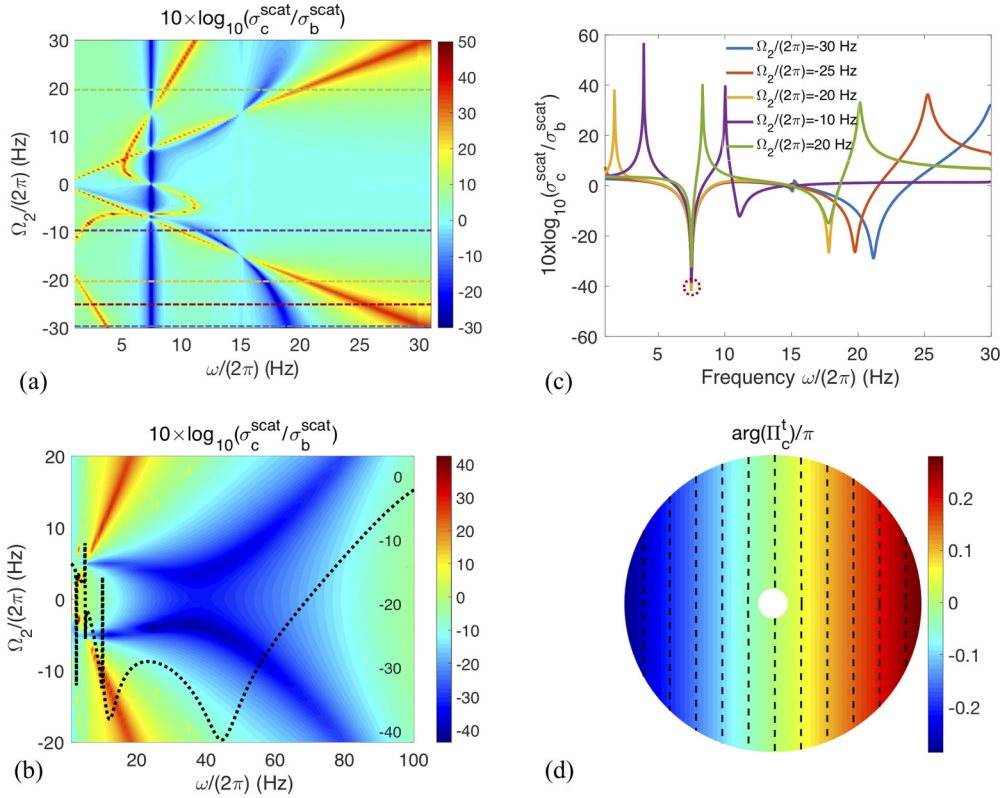

FIG. 9. (a) Normalized SCS ($\sigma_c^{\rm scat}/\sigma_b^{\rm scat}$) in logarithmic scale (where as before the subscripts b and c refer to the SCS of the obstacle and cloaked structure, respectively) vs the wave frequency $\omega/(2\pi)$ and the spinning frequency of the cloaking shell $\Omega_2/(2\pi)$, for $\gamma = 0.71$ and an object of radius 1 m and spinning frequency $\Omega_1/(2\pi) = 15$ Hz, and the same physical parameters as the surrounding, for both object and cloaking shell. The dark blue regions represent the locations of optimized scattering reduction, with values exceeding 30 dB (in absolute value). (b) Same as (a) but here the object has $\rho_1 = \rho_0$ but $\kappa_1 = 0.1 \times \kappa_0$ and moderate spinning $\Omega_1/(2\pi) = 5$ Hz. The shell has the same radius as in (a), $\rho_2 = \rho_0$ but $\kappa_2 = -0.11 \times \kappa_0$. The dashed curve corresponds to a specific $\Omega_2/(2\pi) = -5$ Hz, and its axis is shown. (c) Normalized SCS vs wave frequency $\omega/(2\pi)$ for various values of $\Omega_2/(2\pi)$, corresponding to the dashed colored lines in (a). (d) Phase (normalized with π) of the total Poynting vectors for the cloaked object corresponding to the situation encircled with red dashed line in (c). The black dashed lines represent the contours of the phases.

be modified [57–60,63,80]. If we consider no shear stresses and body forces, it is shown that the momentum conservation can be written as

$$\rho\left(\frac{D\mathbf{u}}{Dt'}\right) = -\nabla' P\,, \tag{B1}$$

where the differential operators D/Dt' and ∇' represent the total time derivative and the spatial derivative, respectively, in the reference frame $\mathcal{R}'$ associated with the spinning disk. The density ρ is assumed to be constant with respect to time due to low compressibility and reasonable rates of rotation, as well as small-amplitude sound waves, as usually assumed. Here the total pressure P accounts for the pressure due to acoustic waves as well as to the rotation of the structure, and $\mathbf{u}$ is the total velocity.

In the reference frame $\mathcal{R}$ associated with the laboratory, Eq. (B1) is transformed into

$$\rho\left[\frac{\partial}{\partial t} + (\mathbf{u}\cdot\nabla)\right]\mathbf{u} = -\nabla P\,, \tag{B2}$$

with $\mathbf{u} = \mathbf{u}_0 + \mathbf{v}$, with $\mathbf{v}$ the velocity of the acoustic wave, and $\mathbf{u}_0 = \mathbf{u}_0(\mathbf{r})$ the bulk velocity, with $\mathbf{r}$ being the position vector with origin taken at the center of the rotating frame, which corresponds to rotation. For a uniform spinning, we have $\mathbf{u}_0 = \Omega r \mathbf{e}_\theta$, with $r = |\mathbf{r}|$, $\mathbf{e}_\theta$ the azimuthal unit vector and Ω the angular velocity. By denoting $P = p_0 + p$, with p_0 the time-independent pressure due to the frame motion and p the pressure of the acoustic waves (due to the acoustic perturbation), Eq. (B2) can be expressed as [80]

$$\left[\frac{\partial}{\partial t} + (\mathbf{u}_0\cdot\nabla)\right]\mathbf{v} + (\mathbf{v}\cdot\nabla)\cdot\mathbf{u}_0 = -\rho^{-1}\nabla p\,. \tag{B3}$$

For the mass conservation equation, a similar reasoning permits to show that it can be expressed in the laboratory frame $\mathcal{R}$ as

$$\left[\frac{\partial}{\partial t} + (\mathbf{u}_0\cdot\nabla)\right]p + c^2\rho\nabla\cdot\mathbf{v} = 0\,, \tag{B4}$$

using the fact that $\nabla\cdot\mathbf{u}_0 = 0$ and noting $c = \sqrt{\kappa/\rho}$, with κ the bulk modulus of the structure.

Similarly, the boundary conditions at the interface between two spinning media (or a spinning media and a medium at rest) shall be modified [80]. For instance, the pressure p is continuous across the interface. For the second boundary condition, which is the normal component of the velocity $(\mathbf{n}\cdot\mathbf{v})$ in media at rest, it was shown in Ref. [80] that it should

be replaced in the moving media by the displacement ψ, which is related to the pressure through the modified relation

$$\rho\left(\frac{\partial}{\partial t}+v_{n_1}\frac{\partial}{\partial n_1}\right)\psi_{n_2}=-\frac{\partial p}{\partial n_2}\,, \tag{B5}$$

with $v_{n_1}=\mathbf{v}\cdot\mathbf{n}_1$ and $\psi_{n_2}=\mathbf{\Psi}\cdot\mathbf{n}_2$, where $\mathbf{n}_1$ is the direction of the flow velocity and $\mathbf{n}_2$ is the normal to the considered interface. It is also assumed here that a very thin membrane separates both fluids from mixing and that the spinning of both fluids is thus independent.

[1] E. Yablonovitch, Phys. Rev. Lett. **58**, 2059 (1987).
[2] S. John, Phys. Rev. Lett. **58**, 2486 (1987).
[3] R. Meade, J. N. Winn, and J. Joannopoulos, *Photonic Crystals: Molding the Flow of Light*, 2nd ed. (Princeton University Press, Princeton, NJ, 1995).
[4] H. Benisty, V. Berger, J.-M. Gerard, D. Maystre, and A. Tchelnokov, *Photonic Crystals: Towards Nanoscale Photonic Devices* (Springer, New York, 2008).
[5] J. Knight, T. Birks, P. S. J. Russell, and D. Atkin, Opt. Lett. **21**, 1547 (1996).
[6] P. Russell, Science **299**, 358 (2003).
[7] T. White, B. Kuhlmey, R. McPhedran, D. Maystre, G. Renversez, C. M. De Sterke, and L. Botten, J. Opt. Soc. Am. B **19**, 2322 (2002).
[8] F. Zolla, G. Renversez, A. Nicolet, B. Kuhlmey, S. Guenneau, D. Felbacq, A. Argyros, and S. G. Leon-Saval, *Foundations of Photonic Crystal Fibres* (Imperial College Press, London, 2005).
[9] M. S. Kushwaha, Appl. Phys. Lett. **70**, 3218 (1997).
[10] J. Vasseur, P. A. Deymier, G. Frantziskonis, G. Hong, B. Djafari-Rouhani, and L. Dobrzynski, J. Phys.: Condens. Matter **10**, 6051 (1998).
[11] Y. Tanaka and S.-i. Tamura, Phys. Rev. B **58**, 7958 (1998).
[12] Y. Tanaka, Y. Tomoyasu, and S.-i. Tamura, Phys. Rev. B **62**, 7387 (2000).
[13] X. Zhang and Z. Liu, Appl. Phys. Lett. **85**, 341 (2004).
[14] Z. Yang, J. Mei, M. Yang, N. H. Chan, and P. Sheng, Phys. Rev. Lett. **101**, 204301 (2008).
[15] Z. Liang, M. Willatzen, J. Li, and J. Christensen, Sci. Rep. **2**, 859 (2012).
[16] S. Yang, J. H. Page, Z. Liu, M. L. Cowan, C. T. Chan, and P. Sheng, Phys. Rev. Lett. **88**, 104301 (2002).
[17] Y. Pennec, B. Djafari-Rouhani, J. O. Vasseur, A. Khelif, and P. A. Deymier, Phys. Rev. E **69**, 046608 (2004).
[18] L.-W. Cai and J. Sánchez-Dehesa, J. Acoust. Soc. Am. **124**, 2715 (2008).
[19] M. Amin, A. Elayouch, M. Farhat, M. Addouche, A. Khelif, and H. Bağcı, J. Appl. Phys. **118**, 164901 (2015).
[20] S. A. Cummer, J. Christensen, and A. Alù, Nat. Rev. Mater. **1**, 16001 (2016).
[21] M. Landi, J. Zhao, W. E. Prather, Y. Wu, and L. Zhang, Phys. Rev. Lett. **120**, 114301 (2018).
[22] Y. Wu, M. Yang, and P. Sheng, J. Appl. Phys. **123**, 090901 (2018).
[23] B. Assouar, B. Liang, Y. Wu, Y. Li, J.-C. Cheng, and Y. Jing, Nat. Rev. Mater. **3**, 460 (2018).
[24] P. A. Deymier, *Acoustic Metamaterials and Phononic Crystals* (Springer Science & Business Media, New York, 2013), Vol. 173.
[25] R. V. Craster and S. Guenneau, *Acoustic Metamaterials: Negative Refraction, Imaging, Lensing and Coaking* (Springer Science & Business Media, 2012), Vol. 166.
[26] Z. Liu, C. T. Chan, and P. Sheng, Phys. Rev. B **71**, 014103 (2005).
[27] F. di Cosmo, M. Laudato, and M. Spagnuolo, in *Generalized Models and Non-Classical Approaches in Complex Materials 1* (Springer, New York, 2018), pp. 247–274.
[28] J. B. Pendry, A. J. Holden, W. J. Stewart, and I. Youngs, Phys. Rev. Lett. **76**, 4773 (1996).
[29] J. B. Pendry, A. J. Holden, D. J. Robbins, and W. Stewart, IEEE Trans. Microwave Theory Tech. **47**, 2075 (1999).
[30] J. B. Pendry, Phys. Rev. Lett. **85**, 3966 (2000).
[31] D. R. Smith, W. J. Padilla, D. C. Vier, S. C. Nemat-Nasser, and S. Schultz, Phys. Rev. Lett. **84**, 4184 (2000).
[32] Z. Liu, X. Zhang, Y. Mao, Y. Zhu, Z. Yang, C. T. Chan, and P. Sheng, Science **289**, 1734 (2000).
[33] J. Li and C. T. Chan, Phys. Rev. E **70**, 055602(R) (2004).
[34] G. Papanicolaou, *Wave Propagation in Complex Media* (Springer Science & Business Media, New York, 2012), Vol. 96.
[35] M. Farhat, P.-Y. Chen, S. Guenneau, and S. Enoch, *Transformation Wave Physics: Electromagnetics, Elastodynamics, and Thermodynamics* (CRC Press, Boca Raton, FL, 2016).
[36] M. Farhat, P.-Y. Chen, H. Bağcı, S. Enoch, S. Guenneau, and A. Alu, Sci. Rep. **4**, 4644 (2014).
[37] S. Brûlé, S. Enoch, and S. Guenneau, Phys. Lett. A **384**, 126034 (2020).
[38] M. Farhat, S. Enoch, S. Guenneau, and A. V. Movchan, Phys. Rev. Lett. **101**, 134501 (2008).
[39] G. Dupont, O. Kimmoun, B. Molin, S. Guenneau, and S. Enoch, Phys. Rev. E **91**, 023010 (2015).
[40] J. Park, J. R. Youn, and Y. S. Song, Phys. Rev. Lett. **123**, 074502 (2019).
[41] S. Zou, Y. Xu, R. Zatianina, C. Li, X. Liang, L. Zhu, Y. Zhang, G. Liu, Q. H. Liu, H. Chen *et al.*, Phys. Rev. Lett. **123**, 074501 (2019).
[42] B. Ungureanu, S. Guenneau, Y. Achaoui, A. Diatta, M. Farhat, H. Hutridurga, R. V. Craster, S. Enoch, and S. Brûlé, EPJ Appl. Metamaterials **6**, 18 (2019).
[43] L. Bennetts, M. Peter, and R. V. Craster, J. Fluid Mech. **854**, R4 (2018).
[44] J. B. Pendry, D. Schurig, and D. R. Smith, Science **312**, 1780 (2006).
[45] U. Leonhardt, Science **312**, 1777 (2006).
[46] F. Zolla, S. Guenneau, A. Nicolet, and J. Pendry, Opt. Lett. **32**, 1069 (2007).
[47] W. F. Bahret, IEEE Trans. Aerosp. Electron. Syst. **29**, 1377 (1993).
[48] T. R. Neil, Z. Shen, D. Robert, B. W. Drinkwater, and M. W. Holderied, J. R. Soc., Interface **17**, 20190692 (2020).
[49] W. Cai, U. K. Chettiar, A. V. Kildishev, and V. M. Shalaev, Nat. Photonics **1**, 224 (2007).
[50] M. Farhat, S. Guenneau, A. Movchan, and S. Enoch, Opt. Express **16**, 5656 (2008).

[51] T. Ergin, N. Stenger, P. Brenner, J. B. Pendry, and M. Wegener, Science **328**, 337 (2010).
[52] A. Alù and N. Engheta, Phys. Rev. E **72**, 016623 (2005).
[53] P.-Y.Chen, J. Soric, and A. Alu, Adv. Mater. **24**, OP281 (2012).
[54] H. Chen and C. Chan, Appl. Phys. Lett. **91**, 183518 (2007).
[55] G. Dupont, M. Farhat, A. Diatta, S. Guenneau, and S. Enoch, Wave Motion **48**, 483 (2011).
[56] J. Xu, X. Jiang, N. Fang, E. Georget, R. Abdeddaim, J.-M. Geffrin, M. Farhat, P. Sabouroux, S. Enoch, and S. Guenneau, Sci. Rep. **5**, 10678 (2015).
[57] E. Graham and B. Graham, J. Acoust. Soc. Am. **46**, 169 (1969).
[58] D. Censor and J. Aboudi, J. Sound Vib. **19**, 437 (1971).
[59] M. Schoenberg and D. Censor, Q. Appl. Math. **31**, 115 (1973).
[60] D. Censor and M. Schoenberg, Appl. Sci. Res. **27**, 401 (1973).
[61] P. Peng, J. Mei, and Y. Wu, Phys. Rev. B **86**, 134304 (2012).
[62] M. P. Lavery, F. C. Speirits, S. M. Barnett, and M. J. Padgett, Science **341**, 537 (2013).
[63] S. Farhadi, J. Sound Vib. **428**, 59 (2018).
[64] D. Ramaccia, D. L. Sounas, A. Alù, A. Toscano, and F. Bilotti, IEEE Trans. Antennas Propag. **68**, 1607 (2019).
[65] Y. Mazor and B. Z. Steinberg, Phys. Rev. Lett. **123**, 243204 (2019).
[66] D. Zhao, Y.-T. Wang, K.-H. Fung, Z.-Q. Zhang, and C. T. Chan, Phys. Rev. B **101**, 054107 (2020).
[67] B. Z. Steinberg, A. Shamir, and A. Boag, Phys. Rev. E **74**, 016608 (2006).
[68] R. Novitski, B. Z. Steinberg, and J. Scheuer, Opt. Express **22**, 23153 (2014).
[69] B. Z. Steinberg, Phys. Rev. E **71**, 056621 (2005).
[70] B. Z. Steinberg and A. Boag, J. Opt. Soc. Am. B **24**, 142 (2007).
[71] D. Ramaccia, D. L. Sounas, A. Alù, A. Toscano, and F. Bilotti, Phys. Rev. B **95**, 075113 (2017).
[72] D. Ramaccia, D. L. Sounas, A. Alù, F. Bilotti, and A. Toscano, IEEE Antennas Wireless Propagation Letters **17**, 1968 (2018).
[73] B. Liu, H. Giddens, Y. Li, Y. He, S. W. Wong, and Y. Hao, Optics Express **28**, 3745 (2020).
[74] M. W. McCall, A. Favaro, P. Kinsler, and A. Boardman, J. Opt. **13**, 024003 (2010).
[75] M. Fridman, A. Farsi, Y. Okawachi, and A. L. Gaeta, Nature (London) **481**, 62 (2012).
[76] M. D. Guild, M. R. Haberman, and A. Alù, J. Acoust. Soc. Am. **128**, 2374 (2010).
[77] M. Farhat, P.-Y. Chen, S. Guenneau, S. Enoch, and A. Alu, Phys. Rev. B **86**, 174303 (2012).
[78] R. Fleury and A. Alù, Phys. Rev. B **87**, 045423 (2013).
[79] M. Farhat, P.-Y. Chen, S. Guenneau, H. Bağcı, K. N. Salama, and A. Alu, Proc. R. Soc. London A **472**, 20160276 (2016).
[80] P. M. Morse and K. Uno Ingard, *Theoretical Acoustics* (Princeton University Press, Princeton, NJ, 1968).
[81] E. Landau, *Handbuch der Lehre von der Verteilung der Primzahlen* (B. G. Teubner, Leipzig, 1909).
[82] Y. Wu, J. Li, Z.-Q. Zhang, and C. T. Chan, Phys. Rev. B **74**, 085111 (2006).
[83] M. Farhat, P.-Y. Chen, S. Guenneau, K. N. Salama, and H. Bağcı, Phys. Rev. B **95**, 174201 (2017).
[84] K. F. Graff, *Wave Motion in Elastic Solids* (Courier Corporation, North Chelmsford, MA, 2012).
[85] Matlab, R2019a, https://www.mathworks.com/
[86] C. Tang and G. A. McMechan, Geophysics **83**, S365 (2018).

Correction: Equation (2) contained a minor typographical error and has been fixed.